

Journal of Materials Chemistry C

Materials for optical, magnetic and electronic devices

Accepted Manuscript

This article can be cited before page numbers have been issued, to do this please use: W. Zhao, G. Zhang, P. Li, L. He, W. Zhu, L. Li, H. Li, Q. Zhang, Z. Guo and X. Liu, *J. Mater. Chem. C*, 2026, DOI: 10.1039/D6TC00764C.



This is an Accepted Manuscript, which has been through the Royal Society of Chemistry peer review process and has been accepted for publication.

Accepted Manuscripts are published online shortly after acceptance, before technical editing, formatting and proof reading. Using this free service, authors can make their results available to the community, in citable form, before we publish the edited article. We will replace this Accepted Manuscript with the edited and formatted Advance Article as soon as it is available.

You can find more information about Accepted Manuscripts in the [Information for Authors](#).

Please note that technical editing may introduce minor changes to the text and/or graphics, which may alter content. The journal's standard [Terms & Conditions](#) and the [Ethical guidelines](#) still apply. In no event shall the Royal Society of Chemistry be held responsible for any errors or omissions in this Accepted Manuscript or any consequences arising from the use of any information it contains.

1 **A Superhydrophobic Bilayer Anisotropic Conductive Film** 2 **with Improved Reliability for Electronic Interconnects**

3 *Wei Zhao^{a,b}, Guoxiang Zhang^{a,b}, Peipei Li^{a,b*}, Libo He^c, Wenfeng Zhu^d, Lei Li^d, Houbu*
4 *Li^d, Qi Zhang^e, Zhanchen Guo^{a*}, Xiaowei Liu^{f*}*

5 *^a Shaanxi Key Laboratory of High-Orbits-Electron Materials and Protection*
6 *Technology for Aerospace, School of Advanced Materials and Nanotechnology, Xidian*
7 *University, Xi'an, Shaanxi, 710071, P.R. China.*

8 *^b State Key Laboratory of Electromechanical Integrated Manufacturing of High-*
9 *performance Electronic Equipments,*
10 *Xidian University, Xi'an, Shaanxi, 710071, P.R. China.*

11 *^c Shanghai Aerospace Resin based Composite Engineering Technology & Research*
12 *Center, Shanghai Composites Science & Technology Co., Ltd., Shanghai, 201112, P.R.*
13 *China.*

14 *^d Tubular Goods Research Institute, China National Petroleum Corporation & State*
15 *Key Laboratory of Oil and Gas Equipment, Xi'an, Shaanxi, 710065, P.R. China.*

16 *^e Zhengzhou Tobacco Research Institute, China National Tobacco Corporation,*
17 *Zhengzhou, Henan, 450001, P.R. China.*

18 *^f Division of Physical Science and Engineering, King Abdullah University of Science*
19 *and Technology, Thuwal 23955-6900, Kingdom of Saudi Arabia.*

20 **Email: lip@xidian.edu.cn (P. Li), guozhanchen@xidian.edu.cn (Z. Guo), and*
21 *xiaowei.liu@kaust.edu.sa (X. Liu)*

22



23 Abstract

24 Anisotropic conductive films (ACFs) are essential interconnect materials in flexible,
25 high-density electronics but suffer from low functional reliability under humid or
26 contaminated conditions. A superhydrophobic bilayer ACF (S-ACF) is developed to
27 address this limitation through a scalable spray-coating process that deposits a
28 composite of vapor-phase SiO₂ nanoparticles and styrene-ethylene-butylene-styrene
29 (SEBS) onto a conventional epoxy-based ACF. The resulting film exhibits a dual-layer
30 architecture in which the SiO₂/SEBS topcoat forms a micro–nano hierarchical texture
31 with low surface energy, yielding a static water contact angle of 150° compared to 64°
32 for the pristine ACF. Despite the surface modification, the bonding strength (17.1 MPa)
33 and Z-axis contact resistance (1.64 Ω) remained nearly identical to those of the
34 unmodified counterpart (17.2 MPa, 1.58 Ω). Additionally, the minimum lateral
35 insulation distance of the S-ACF was approximately 60 μm, confirming that both the
36 mechanical and electrical integrity were preserved. The superhydrophobic surface
37 endures over 200 abrasion and tape-peel cycles while retaining ≥145° contact angle and
38 exhibits a twofold reliability enhancement in humid-heat stability (85 °C/85% RH,
39 resistance inflection shifted from ~150 to ~300 hours). The design in this work offers a
40 practical route toward durable, moisture-resistant interconnects for next-generation
41 flexible electronics.

42 **Keywords:** Bilayer Anisotropic Conductive Film, Superhydrophobicity, Anisotropic
43 Conductivity, Mechanical Robustness, Improved Reliability

44 1. Introduction

45 Electronic components are rapidly evolving toward greater integration, flexibility,
46 and miniaturization, driven by emerging applications ranging from drones¹⁻³ and high-
47 resolution displays,⁴⁻⁶ to implantable medical devices,⁷⁻⁹ robotic electronic skin,^{10, 11}
48 and flexible human–machine interfaces.¹²⁻¹⁵ The role of electronic packaging in modern
49 electronic systems has become increasingly critical. Among various interconnection



50 approaches, flip-chip bonding has emerged as a mainstream technology for high-
51 density, fine-pitch packaging owing to its reduced interconnect pitch and streamlined
52 processing. In current flip-chip assembly, interconnect materials are predominantly
53 metallic solders, with conventional Sn-Pb solder being a representative example.^{16, 17}
54 However, flip chip bonding using metallic solders can only achieve a minimum bonding
55 interconnect pitch of several hundred micrometers, making it difficult to meet the
56 demands for high density and flexibility in device development.^{18, 19} Consequently,
57 developing novel bonding interconnect materials has become an imperative
58 requirement to overcome this challenge.

59 Anisotropic conductive film (ACF) serves as a key interconnect medium that
60 provides out-of-plane (z-axis) electrical conduction while ensuring robust mechanical
61 adhesion.²⁰⁻²² Structurally, ACFs are polymer-particle composites comprising
62 conductive microspheres (MPs) dispersed in an insulating matrix (e.g., epoxy or acrylic
63 resins).²³⁻²⁵ During hot-pressing, the MPs are compressed to form vertical conductive
64 paths between opposing contact pads, while the cured adhesive maintains the deformed
65 state of the conductive particles and ensures stable electrical contact with the mating
66 electrodes, simultaneously preserving lateral insulation. This synergy of particle
67 architecture and cross-linked polymer networks results in robust interfacial adhesion
68 and toughness across diverse substrates, meeting the stringent requirements of low
69 contact resistance and mechanical reliability of fine-pitch assemblies. To further
70 enhance electrical performance of ACFs, recent efforts have focused on optimizing
71 particle arrangement and composition. For instance, Cao et al. used transient emulsion
72 self-assembly and nanosecond-laser processing to rapidly fabricate pure-Au
73 microsphere arrays within photolithographic templates, creating arrayed ACFs with
74 stable conduction under deep-press conditions.²⁶ Park et al. employed UV soft-template
75 patterning and frictional alignment to precisely position Au-coated PS microspheres in
76 an elastomeric matrix, producing ordered, stretchable ACFs resistant to particle
77 migration.²⁷ Similarly, Hao et al. introduced a polyaniline (PANI) intermediate layer to
78 streamline Ag plating on polystyrene (PS) beads, forming PS@PANI@Ag



79 microspheres; through template-friction assembly, they fabricated arrayed ACFs that
80 achieved a low interconnection of 1.78Ω and retained conductivity after 120 hours of
81 testing at $85^\circ\text{C}/85\% \text{RH}$.²⁸ While these advances in particle engineering, matrix
82 optimization, and deterministic ordering significantly enhance contact formation and
83 adhesion, they do not fundamentally address the root causes of low interface reliability.
84 In practical environments—such as humid-heat aging, thermal cycling, and repeated
85 bending—moisture exposure, surface contaminant accumulation, and electrochemical
86 reactions can still trigger contact resistance drift and circuit failure. Consequently,
87 ensuring long-term reliability under these mechanically and humid-heat conditions
88 remains a challenge for ACF-based interconnect technologies.

89 Among the available strategies to improve environmental and interfacial reliability,
90 superhydrophobic coatings with micro–nano hierarchical textures offer a compelling
91 solution by blocking moisture ingress, suppressing electrochemical corrosion, and
92 minimizing residue accumulation.^{29–33} These surfaces combine large static contact
93 angles with small roll-off angles, imparting anti-fouling and self-cleaning properties.
94 Their multiscale architectures trap air pockets that reduce the effective solid–liquid
95 contact area and surface free energy, enabling droplets to detach rapidly in a "ball-like"
96 fashion and providing durable protection under harsh conditions. Representative studies
97 demonstrate their robustness. Wang et al. densely embedded near-zero-shrinkage
98 superhydrophobic silica aerogels into rigid Fe–Ni foams with regular dodecahedral
99 units, followed by fluorination.³⁴ The obtained interpenetrating composite sustained
100 $\sim 7.4 \text{ MPa}$ compressive strength at 8 % strain, exhibited minimal wear ($\approx 0.567 \text{ mm}^3$)
101 after 5000 abrasion cycles, and maintained performance under extreme temperature,
102 humidity, pressure, and abrasion. In a flexible context, Zhang et al. developed
103 superhydrophobic and highly stretchable films by blending vulcanized natural latex
104 with a silicone emulsion, followed by surface modification; these films preserved
105 superhydrophobicity at 500% tensile strain and maintained water contact angles above
106 155° after 300 cycles at 300% strain.³⁵ Collectively, these studies demonstrate that



107 robust hydrophobic barriers can remain functionality under coupled mechanical and
108 environmental stressors.

109 Building on these advances, we developed a superhydrophobic bilayer anisotropic
110 conductive film (S-ACF) by applying a conformal SiO₂@SEBS nanocomposite topcoat
111 to an original ACF. This top layer confers stable water repellency, elevating the water
112 contact angle from 64° to 150°, which effectively suppresses moisture absorption and
113 surface contamination. SEBS was selected as the binder for the superhydrophobic
114 coating because it offers good processability, flexibility, and cyclohexane solubility,
115 enabling uniform spray coating. In addition, its fluorine-free nature makes it relatively
116 environmentally friendly and suitable for practical electronic packaging application.
117 Notably, the bilayer configuration retains the core mechanical and electrical
118 performance of the base ACF, with negligible change in lap-shear strength (17.2→17.1
119 MPa) and z-axis resistance (1.58→1.64 Ω). Most importantly, under 85 °C/85% RH
120 testing, the onset of resistance rise is delayed from 150 to 300 hours, indicating a
121 twofold enhancement in operational lifetime against moisture-induced failure. In
122 addition, peel-resistance and abrasion tests were conducted, during which the cured S-
123 ACF maintained a water contact angle of ≥145° even after 200 test cycles, indicating
124 excellent mechanical robustness of the superhydrophobic surface. Overall, this work
125 introduces a simple, scalable, and materials-compatible strategy to countering key
126 failure of low reliability under humid or contaminated conditions in ACFs, paving the
127 way for durable, fine-pitch interconnects in flexible electronics and wearable systems.

128 2. Experimental

129 2.1 Materials

130 Hydrochloric acid (HCl, 37%), aqueous ammonia (NH₃·H₂O, 25%-28%), Ethyl
131 alcohol (C₂H₅OH, Analytical Reagent), cyclohexane (C₆H₁₂, Analytical Reagent) and
132 tetrahydrofuran (THF) were obtained from Sinopharm Chemical Reagent Co., Ltd.
133 Silver nitrate (AgNO₃, Analytical Reagent), glucose (C₆H₁₂O₆, Analytical Reagent),
134 potassium sodium tartrate (NaKC₄H₄O₆, Analytical Reagent), tin(II) chloride dihydrate



135 (SnCl₂·2H₂O, Analytical Reagent), 3-glycidoxypropyltrimethoxysilane (KH560) were
136 provided by Shanghai Macklin Biochemical Co., Ltd. Silica (SiO₂, 10 μm) was
137 supplied by Orite New Materials. Fumed silica was provided by Hubei Huifu Nano
138 Materials Co., Ltd. Thermoplastic polyurethane (TPU) was provided by Yuanding
139 Plastics Co., Ltd. Styrene ethylene butylene styrene (SEBS) was provided by Shangsu
140 Technology Co., Ltd. Epoxy resin (E51) was provided by Shanghai Macklin
141 Biochemical Technology Co., Ltd. The curing agent (Latent, HS-604) was provided by
142 Chuzhou Huisheng Electronic Materials Co., Ltd. All chemicals were used as received,
143 without further purification.

144 2.2 Preparation of the SiO₂@Ag Conductive Fillers

145 The SiO₂@Ag conductive fillers were synthesized via an electroless plating
146 method. Briefly, SiO₂ particles were dispersed in ethanol to form an uniform
147 suspension. The particles were sensitized by adding a solution of SnCl₂·2H₂O in
148 hydrochloric acid, followed by magnetic stirring and filtration to obtain Sn²⁺-adsorbed
149 silica. Separately, a silver ammonia solution was prepared by adding ammonia
150 dropwise to an aqueous AgNO₃ solution until the initial precipitate dissolved. The
151 sensitized SiO₂ particles were then introduced into the silver ammonia solution under
152 stirring. Subsequently, an aqueous mixture of glucose and potassium sodium tartrate
153 was added dropwise as a reducing agent, leading to the deposition of silver
154 nanoparticles onto the SiO₂ surfaces, as indicated by a color change to black. The
155 resulting SiO₂@Ag nanoparticles were isolated by repeated washing with deionized
156 water and dried thoroughly.³⁶

157 2.3 Preparation of the Superhydrophobic Bilayer Anisotropic Conductive Film (S- 158 ACF)

159 The superhydrophobic bilayer anisotropic conductive film (S-ACF) was fabricated
160 by spray-coating a hydrophobic top layer onto a pre-stretched base ACF. First, the
161 epoxy resin and TPU were first thoroughly mixed at a mass ratio of 1:1 and dispersed
162 in tetrahydrofuran. Subsequently, SiO₂@Ag conductive particles and a latent curing
163 agent were added. The original ACF was prepared by doctor-blading a mixture of epoxy



164 resin, curing agent, and SiO₂@Ag conductive filler (mass ratio=10:8:7) in solvent onto
165 a PTFE film.³⁶ Under the formulation used in this work, the volume fraction of
166 SiO₂@Ag conductive fillers in the adhesive matrix is estimated to be ~8-9 vol%, based
167 on typical densities of the epoxy matrix (~1.2 g·cm⁻³) and SiO₂@Ag core-shell
168 particles (~5.0 g·cm⁻³). A blade gap of 150 μm and a coating speed of 10 mm/s were
169 used, followed by lamination with a release liner. The ACF was then uniaxially
170 stretched to 150 % of its original length and fixed in position. Prior to spray-coating,
171 the ACF was stretched to expose surface grooves and valleys on the originally non-
172 smooth ACF surface, which facilitates more uniform coverage of the superhydrophobic
173 layer. The hydrophobic coating solution was formulated by dissolving vapor-phase
174 SiO₂ in cyclohexane, followed by sonication and stirring, after which SEBS was added.
175 This SiO₂/SEBS solution was sprayed onto the stretched ACF using a spray gun at a
176 pressure of 0.2 MPa, a distance of 10–15 cm, and a traverse speed of approximately 5
177 cm/s. After complete solvent evaporation, the film was released to recover its original
178 dimensions, yielding the final S-ACF with a conformal superhydrophobic surface.

179 2.4 Measurements

180 The surface morphology of samples was characterized using a scanning electron
181 microscope (SEM, Hitachi SU8600). Surface topography and roughness were analyzed
182 with a laser scanning confocal microscope (LSCM, Olympus LEXT OLS5100). The
183 crystal structures of the pristine ACF, superhydrophobic bilayer ACF, fumed silica, and
184 SiO₂ microspheres were determined by X-ray diffraction (XRD, Bruker D8 Advance),
185 while Fourier transform infrared spectroscopy (FTIR, Thermo Scientific) identified
186 chemical functional groups. Static water contact angles were measured using an optical
187 goniometer (Biolin Scientific TFL400) with 4 μL droplets of deionized water dispensed
188 from a height of 1 cm. A high-speed camera (YVISION OSG030-815UCTZ, 300 fps)
189 captured the dynamic droplet-surface interactions during contact-angle measurement.
190 Abrasion resistance was evaluated by sliding a 100 g weight attached to the sample
191 across a 10 cm path on 2000-grit sandpaper, where one back-and-forth motion was
192 counted as one cycle. Peel resistance was tested by adhering 3M 810 tape to the surface,



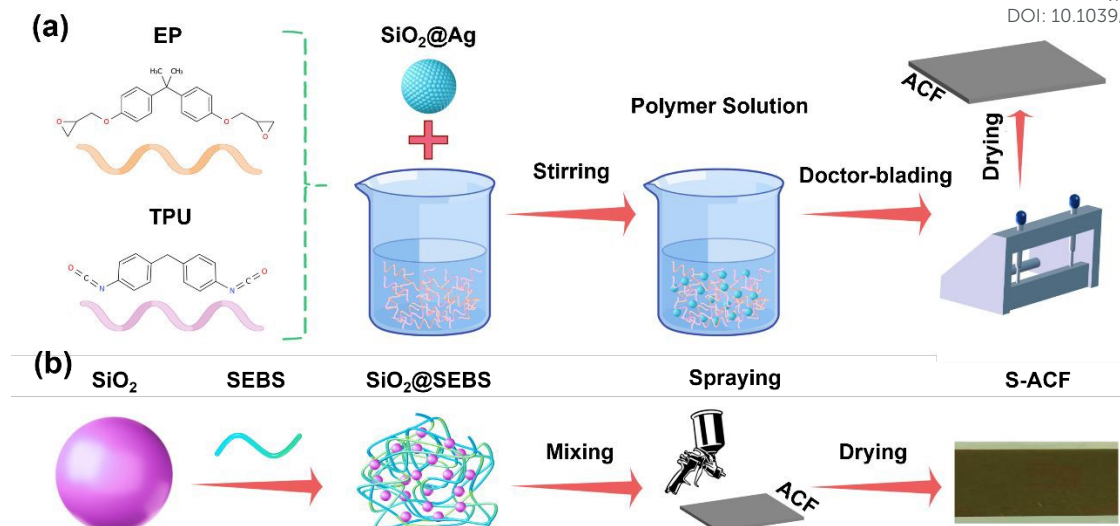
193 pressing with a 200 g weight, and subsequently peeling it off. Stain resistance was
194 assessed by immersing samples in a red ink aqueous solution for 1 minute. Bonding
195 strength were analyzed according to the GB/T 7124-2008 standard using a universal
196 testing machine (ZM-30000N).³⁷ Copper tape specimens (40 mm×10 mm×0.3 mm)
197 with an overlap area of 10 mm×5 mm was cured at 150 °C for 60 minutes, and tested
198 at a loading rate of 10 mm/min. Tensile strength and elongation at break were measured
199 per GB/T 2567-2008 at the same loading rate.³⁸ For all mechanical tests, five parallel
200 samples were assessed, and results are reported as the mean ± standard deviation. Using
201 two pieces of 40 mm×10 mm×0.3 mm copper sheets, sandwiching 10 mm×5 mm S-
202 ACF in the middle, hot pressing for 10 minutes under 0.3 MPa and 150°C conditions,
203 and then curing for one hour at 150°C, the bonding test sample can be prepared. Cut the
204 S-ACF into a 10 mm×50 mm rectangle and cure it at 150°C for one hour to obtain the
205 tensile test sample. Specific test diagrams are shown in Figure S1 and S2. Electrical
206 properties were evaluated using a test structure composed of an ACF layer hot-pressed
207 between two polyimide (PI) films with patterned silver electrodes. Bonding tests were
208 carried out at 150°C under a pressure of 0.3 MPa for 10 min using Ag electrodes
209 patterned on PI films with a fixed electrode spacing of 1 mm. The bonded assembly
210 was then fully cured at 150 °C for 1 h, after which the electrical properties were
211 measured directly using a standard ohmmeter: the resistance between the top and
212 bottom electrodes was used to evaluate Z-axis electrical conduction, while the
213 resistance between laterally separated electrodes was used to assess X-Y directional
214 electrical insulation. The specific contact resistance test schematic is shown in Figure
215 S3. Unless otherwise stated, all ACF and S-ACF samples were fully cured prior to any
216 characterization. All wettability, surface morphology, mechanical, and electrical
217 measurements reported in this work were conducted on cured samples.

218

219 3. Results and discussion

220 3.1. Preparation and Characterization of S-ACF





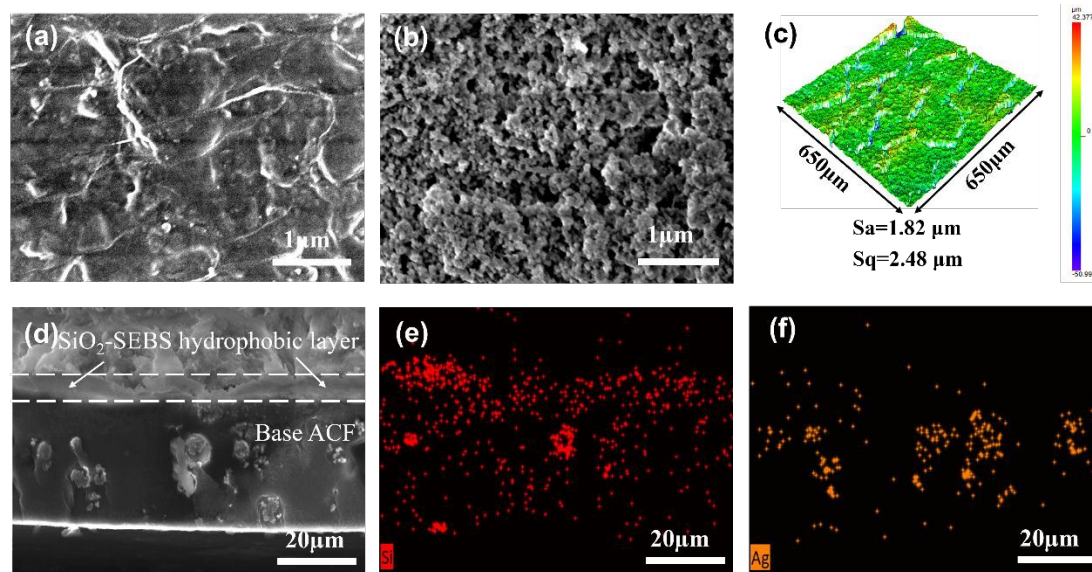
221

222 **Figure 1.** Schematic illustration of the fabrication process for (a) the base ACF and (b)
 223 the superhydrophobic bilayer anisotropic conductive film (S-ACF).

224 The base ACF was first synthesized on a release film via a tape-casting process.
 225 As shown in Figure 1a, this original ACF consisted of silver-coated SiO_2 microspheres
 226 as conductive fillers dispersed in an epoxy resin matrix with a latent curing agent. The
 227 epoxy resin and TPU were first thoroughly mixed at a mass ratio of 1:1 and dispersed
 228 in tetrahydrofuran. Subsequently, $\text{SiO}_2@Ag$ conductive particles and a latent curing
 229 agent were added. The original ACF was prepared by doctor-blading a mixture of epoxy
 230 resin, curing agent, and $\text{SiO}_2@Ag$ conductive filler (mass ratio=10:8:7) in solvent onto
 231 a PTFE film.³⁶ The silver-coated SiO_2 spheres were synthesized in-house, and their
 232 successful formation was verified by X-ray diffraction (XRD) and scanning electron
 233 microscopy (SEM). The XRD pattern (Figure S4a) of pristine SiO_2 shows a broad
 234 diffraction peak at $\sim 20^\circ$, confirming its amorphous structure. Following silver coating,
 235 distinct peaks at 38.1° , 44.3° , 64.4° , and 77.4° emerged, corresponding to the (111),
 236 (200), (220), and (311) planes of face-centered cubic silver, respectively, consistent
 237 with standard reference data. SEM images (Figure S4b and S4c) provide
 238 complementary morphological evidence: the pristine SiO_2 spheres are smooth and
 239 uniform, whereas the silver-coated spheres maintain their spherical shape but exhibit a
 240 roughened surface covered with granular features, which are attributed to Ag
 241 nanoparticles deposited on the SiO_2 surface rather than a continuous coating layer.



242 These nanograins are attributed to metallic Ag crystallites, confirming successful silver
 243 layer deposition. To construct the superhydrophobic bilayer, the ACF surface was
 244 finally spray-coated with a cyclohexane solution containing vapor-phase SiO₂
 245 nanoparticles and SEBS. Upon solvent evaporation, a conformal topcoat with micro-
 246 nano-scale roughness and intrinsically low surface energy was formed, completing the
 247 S-ACF structure, as illustrated in Figure 1b.



248
 249 **Figure 2.** Morphological and elemental characterization of cured ACF and S-ACF. (a,
 250 b) Top-surface SEM images of (a) ACF and (b) S-ACF. (c) LSCM image of the S-ACF
 251 surface. (d) Cross-sectional SEM image revealing the internal structure of S-ACF. (e,
 252 f) Corresponding EDS elemental maps of the S-ACF cross-section.

253 The surface of the unmodified ACF appears relatively smooth and compact. As
 254 shown in the SEM image (Figure 2a), only shallow grooves and slight undulations are
 255 visible, which likely arise from epoxy curing shrinkage. This morphology lacks the
 256 hierarchical micro-nano-scale roughness required to induce superhydrophobicity. In
 257 contrast, the SiO₂/SEBS-modified surface (Figure 2b) reveals a densely packed coating
 258 of micro-nano-structured particles, forming a highly rough and porous texture
 259 favorable for water repellence.^{39, 40} The three-dimensional profile obtained by laser
 260 scanning confocal microscopy (LSCM, Figure 2c) shows a continuous hierarchical
 261 topology composed of nano-steps and protrusions, with an arithmetic average



262 roughness (S_a) of approximately $1.82\ \mu\text{m}$ and a root mean square height (S_q) of
263 approximately $2.48\ \mu\text{m}$. Such engineered roughness is critical for superhydrophobicity,
264 as the hierarchical structures trap a stable layer of air within their cavities, generating a
265 gas film at the liquid-solid interface. This air film acts as a physical barrier, preventing
266 direct contact between water and the ACF surface, thereby significantly enhancing its
267 corrosion resistance. Simultaneously, the inherent low surface energy of the vapor-
268 phase SiO_2 further reduces interfacial free energy. The synergistic effect of surface
269 roughness and low energy minimizes the solid-liquid contact area, leading to nearly
270 spherical water droplets characterized by a high contact angle and robust
271 hydrophobicity behavior.

272 Cross-sectional analysis of the S-ACF provides further insight into its structure.
273 The SEM image (Figure 2d) reveals a distinct, continuous SiO_2/SEBS top layer that
274 forms a clear interface with the underlying ACF. This topcoat adheres tightly to the
275 epoxy matrix without delamination or voids and exhibits internal protrusions consistent
276 with the micro-nano-scale roughness observed on the surface. Such a bilayer
277 architecture underpins the material's dual functionality. The dense, rough top layer
278 confers superhydrophobicity and antifouling capability, while its thinness and elasticity
279 —attributed to the SEBS elastomer—ensure that it does not impede the penetration of
280 conductive particles during hot-pressing. As a result, reliable z-axis conductive
281 pathways are maintained, preserving the ACF's anisotropic conductivity, as
282 corroborated by subsequent electrical characterization. Elemental mapping via EDS
283 further verifies this stratified design: the Si distribution (Figure 2e) is concentrated in
284 the surface region, confirming the enrichment of vapor-phase SiO_2 nanoparticles,
285 where the isolated Si signals within the ACF bulk originate from Ag-coated SiO_2 fillers.
286 Conversely, the Ag signal (Figure 2f) is predominantly localized at these filler sites
287 within the conductive layer, illustrating that the current-carrying network remains intact
288 beneath the hydrophobic shield. This clearly defined “hydrophobic-conductive” dual-
289 layer structure provides the structural basis for achieving hydrophobicity.

290



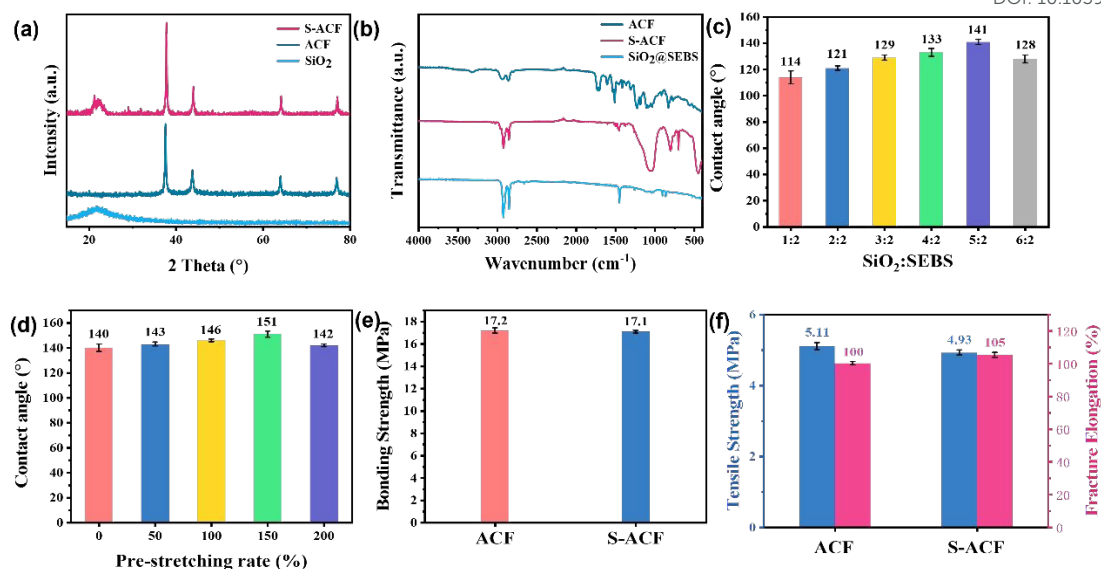
291 3.2. Hydrophobic and Mechanical Properties of S-ACF

View Article Online
DOI: 10.1039/D6TC00764C

292 To further validate the successful construction of the S-ACF bilayer, we performed
293 X-ray diffraction (XRD) and Fourier-transform infrared (FTIR) spectroscopy (Figure
294 3a-b). In the XRD patterns (Figure 3a), the diffraction peaks corresponding to the Ag-
295 coated SiO₂ fillers remain identical to those discussed above, indicating that their
296 crystalline structure as conductive components within the ACF matrix is fully preserved.
297 After modification, an additional amorphous scattering feature near $2\theta \approx 20^\circ$ becomes
298 evident, attributable to the SiO₂-containing top layer, further supporting the successful
299 introduction of the hydrophobic coating. Notably, no discernible peak shift or
300 broadening is observed, indicating that the modification does not introduce measurable
301 lattice distortion or micro strain in the Ag fillers. The retention of both peak intensity
302 and sharpness implies that the hydrophobic SiO₂/SEBS overlayer is thin and exerts
303 negligible influence on the diffraction from the underlying conductive network,
304 aligning with the intended bilayer design in which electrical pathways through Ag are
305 maintained. FTIR spectra (Figure 3b) provide complementary evidence for this bilayer
306 configuration. The SiO₂@SEBS coating exhibits a C-H stretching band from SEBS
307 near 2900 cm⁻¹ and a pronounced Si-O absorption centered around 1100 cm⁻¹,
308 dominated by Si-O-Si asymmetric stretching characteristic of vapor-phase SiO₂.
309 Compared with the unmodified ACF, the S-ACF spectrum shows a markedly enhanced
310 C-H stretching signal (~ 2900 cm⁻¹), indicating the presence of the organic SEBS
311 component, and an intensified Si-O band (~ 1100 cm⁻¹), reflecting the enrichment of
312 SiO₂ at the outer surface following cyclohexane evaporation during modification.
313 Together, the XRD and FTIR results consistently demonstrate the successful deposition
314 of a SiO₂-containing hydrophobic overlayer on the ACF while preserving the
315 crystalline integrity and electrical continuity of the Ag-based conductive network. This
316 confirms that the surface modification imparts hydrophobic functionality with minimal
317 impact on the film's electrical performance.

318





319

320 **Figure 3.** Structural and mechanical characterization of the ACF and S-ACF. (a) XRD
 321 patterns of ACF, SiO₂, and S-ACF, identifying crystalline phases. (b) FTIR spectra of
 322 ACF, a SiO₂/SEBS mixture, and S-ACF, confirming chemical functionalization. (c)
 323 Water contact angle of S-ACF plotted against increasing SiO₂ filler content. (d)
 324 Water contact angle of S-ACF measured under 0–200% pre-stretching rate. (e) Bonding
 325 strength of the S-ACF. (f) Tensile strength and elongation at break for ACF and S-ACF,
 326 comparing their mechanical performance.

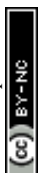
327 In practical applications, the service life of ACFs is often curtailed by ambient
 328 humidity and condensate, as moisture adsorption and penetration can gradually degrade
 329 the polymer matrix and interfacial electrical contacts, leading to increased contact
 330 resistance and reduced reliability. Motivated by the “water-beading” effect of
 331 waterproof textiles and prior work by Wang et al., we implemented a hydrophobic
 332 surface modification to improve environmental stability.⁴¹ We first quantified the effect
 333 of vapor-phase SiO₂ loading on hydrophobicity (Table S1). With SEBS (200 mg) and
 334 cyclohexane (100 mL) kept constant, the SiO₂ dose was varied from 100 to 600 mg
 335 (SiO₂:SEBS=1:2 to 6:2). As shown in Figure 3c, the static contact angle rose
 336 monotonically with SiO₂ content, peaking at the 5:2 formulation (#8 in Table S1, SiO₂
 337 =500 mg) from ~114° to 141°. Beyond this point, the contact angle declined to ~128°
 338 at 6:2. This “rise-then-fall” trend suggests that, moderate particle loadings enable the



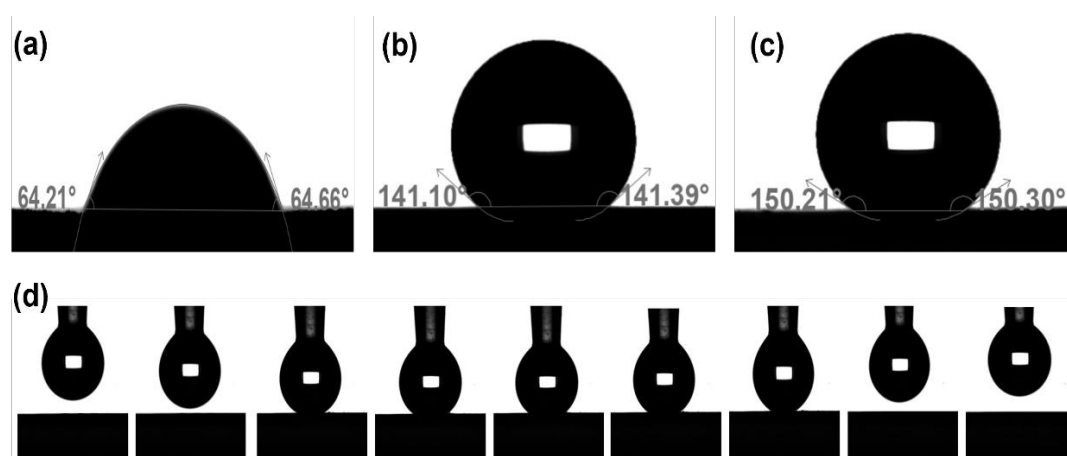
339 formation of continuous micro/nano hierarchical roughness that stabilizes an air
340 cushion, whereas excessive SiO₂ induces local agglomeration, disrupts roughness
341 uniformity, and compromises air-pocket continuity which diminishes hydrophobicity.
342 Consistently, the unmodified ACF shows groove-rich, scale-mismatched topography,
343 limiting its intrinsic water repellence. It should be noted that the water contact angle
344 measurements were performed after complete curing of the ACF, ensuring that the
345 measured wettability reflects the intrinsic surface state of the cured material.

346 Building on this insight, we employed a pre-stretching-assisted spray method to
347 amplify the surface structure. Leveraging the ductility of the epoxy/TPU matrix prior
348 to full cure, the ACF was axially pre-stretched by 50%-200% before SiO₂@SEBS
349 deposition. As summarized in Figure 3d, the contact angle exhibits a non-monotonic
350 dependence on pre-strain: it increases with strain, reaching 150° (superhydrophobic
351 regime) at 150% pre-stretching process, and slightly declines at 200%. We attribute the
352 optimum to strain-mediated “opening” and magnification of surface grooves, which
353 improves coating conformity and fosters favorable micro/nano composite roughness.
354 This interpretation is further supported by the LSCM comparison of the resulting S-
355 ACF surfaces prepared with and without pre-stretching (Figure S5), where the pre-
356 stretched sample exhibits more pronounced groove features and higher areal roughness
357 parameters (Sa and Sq). Over-stretching likely perturbs feature uniformity and/or
358 introduces local defects, weakening the Cassie state. Together, composition tuning
359 (SiO₂:SEBS=5:2) and moderate pre-stretching process (~150%) deliver a robust
360 superhydrophobic surface, providing an effective route to mitigate humidity-induced
361 degradation and extend the service durability of ACFs. Figure S6a and S6b illustrate
362 the anti-soiling and self-cleaning capabilities of S-ACF, underscoring its sustained
363 resistance to moisture and stains during operational use.

364 Meanwhile, we also assessed whether the superhydrophobic modification affects
365 the bulk mechanical properties of the ACF. Figure S7a (after the bonding test) and
366 Figure S7b (after the tensile test) show rough and torn fracture morphologies,
367 accompanied by clear plastic deformation and tearing features. No large-scale



368 delamination of the superhydrophobic surface layer is observed; instead, failure occurs
 369 primarily within the ACF bulk rather than at the interfaces. This indicates that
 370 interfacial adhesion exceeds the cohesive strength of the ACF, leading to crack
 371 propagation through the bulk. In addition, as shown in Figure 3e, the bonding strengths
 372 of the modified and unmodified specimens are 17.2 MPa and 17.1 MPa, respectively—
 373 essentially identical within experimental uncertainty—indicating that the thin
 374 SiO₂@SEBS overlayer does not compromise the cohesive integrity of the adhesive
 375 network or its interfacial bonding. Specific test diagrams are shown in Figure S1 and
 376 S2. Similarly, uniaxial tensile metrics (Figure 3f) were largely preserved: the S-ACF
 377 exhibits an ultimate tensile strength of 4.93 MPa and an elongation at break of 105%,
 378 compared with 5.11 MPa and 100% for the pristine ACF. The near invariance of both
 379 strength and ductility confirms that the hydrophobic coating neither embrittles nor
 380 plasticizes the matrix. These mechanical outcomes are consistent with cross-sectional
 381 SEM imaging (Figure 2d), which reveals an ~3 μm surface layer intimately bonded to
 382 the underlying ACF without interfacial defects or delamination. Collectively,
 383 optimizing the SiO₂ volume fraction and applying the pre-stretching–assisted spray
 384 process enables the tuning of surface wettability into the superhydrophobic regime
 385 while preserving load-bearing and deformability characteristics. This strategy therefore
 386 enhances environmental durability of ACF (e.g., resistance to humidity and condensate)
 387 without compromising mechanical performance.



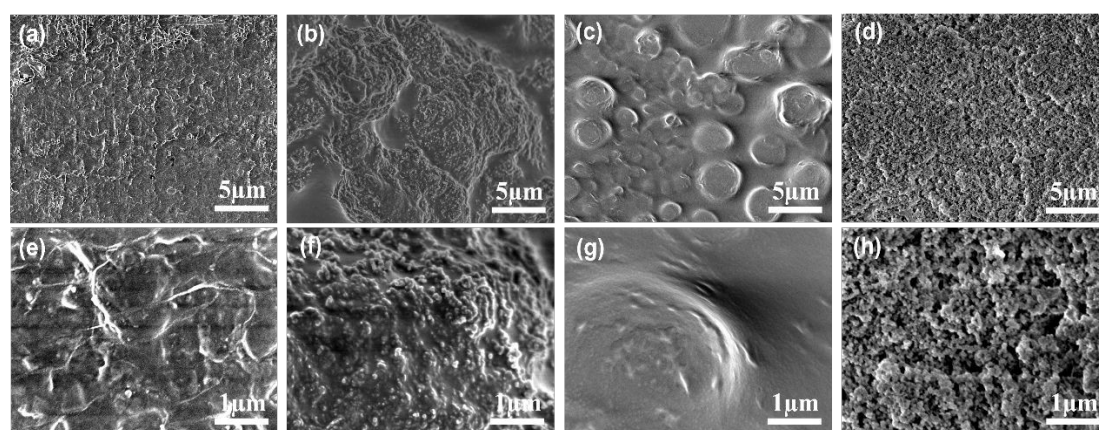
388

389 **Figure 4.** Evaluation of hydrophobic and anti-fouling properties. (a-c) Evolution of the
 390 static water contact angle: (a) pristine ACF, (b) S-ACF, and (c) S-ACF under 150%



391 tensile strain. (d) Dynamic self-cleaning demonstration, where water droplets are
392 unable to adhere to the S-ACF surface and easily roll off. All contact angle
393 measurements were carried out on fully cured ACF and S-ACF samples.

394 To directly compare how each treatment alters wettability, Figure 4 compiles static
395 contact-angle and adhesion behaviors of the samples. Representative optical images of
396 contact angles for the pristine ACF, the unstretched SiO₂@SEBS-modified ACF, and
397 the pre-stretched, spray-coated S-ACF are shown in Figure 4a-c, respectively. The
398 unmodified ACF exhibits a modest static contact angle of 64°, while SiO₂@SEBS
399 modification increases the angle to 141°. Incorporating the pre-stretching-spray-coating
400 step further elevates the angle to 150°, entering the superhydrophobic regime. This
401 progressive improvement aligns with the trend in Figure 3d and substantiates the
402 effectiveness of our synergistic “formulation-pre-stretching-coating” strategy. To
403 assess surface adhesion, a high-speed camera recorded the dynamic “contact-separation”
404 process between a 4 μL water droplet and the film surface (Figure 4d). On the S-ACF,
405 the droplet maintains nearly spherical upon contact and detaches cleanly during needle
406 retraction without residue, indicating extremely weak solid-liquid interfacial adhesion
407 and a canonical low-adhesion superhydrophobic state.



408
409 **Figure 5.** Morphological evolution of the S-ACF. Representative SEM images show:
410 (a, e) the pristine ACF; (b, f) the intermediate state after SiO₂ deposition; (c, g) the
411 subsequent SEBS modification; and (d, h) the final S-ACF.



412 The superior hydrophobicity of the SiO₂-SEBS couple can be rationalized by
413 examining the surface morphologies in Figure 5. Without coating (Figure 5a, 5e), the
414 groove-rich surface lacks a percolating, multiscale texture capable of stably trapping
415 air. Introducing vapor-phase SiO₂ alone (Figure 5b, 5f) leads to “cauliflower-like”
416 agglomeration and poor dispersion; during epoxy softening/curing, these clusters are
417 readily embedded, blunting asperities and suppressing effective micro–nano features at
418 the interface. Applying SEBS alone (Figure 5c, 5g) produces a dense, relatively smooth
419 organic film that fills pre-existing grooves, again preventing air-cushion formation.
420 Only when SiO₂ and SEBS act synergistically (Figure 5d, 5h) does the elastomeric
421 SEBS act as a compliant binder, immobilizing SiO₂ particles that partially protrude at
422 the surface. SEBS also improves SiO₂ dispersion and suppresses agglomeration during
423 spray coating, facilitating the formation of a more uniform micro-/nano-scale
424 hierarchical roughness. In addition, SEBS provides stable anchoring sites that firmly
425 immobilize SiO₂ within the surface layer, reducing particle pull-out and structural
426 damage under repeated mechanical loading, and thereby enhancing the wear resistance
427 of the superhydrophobic coating. This configuration constructs a continuous micro–
428 nano hierarchical roughness with interconnected voids. The interparticle interstices
429 function as air pockets, reducing the real solid-liquid contact area and stabilizing the
430 Cassie state. Concurrently, the SEBS matrix enhances particle anchorage and wear
431 resistance, mitigating pull-out and delamination. As a result, the surface texture - and
432 thus the wetting state - remains stable during repeated use. This composite architecture
433 unites high static contact angles with low adhesion (low hysteresis), delivering the
434 desired low-adhesion superhydrophobic behavior.

435 3.3. Electrical and humid-heat Reliability Properties of S-ACF

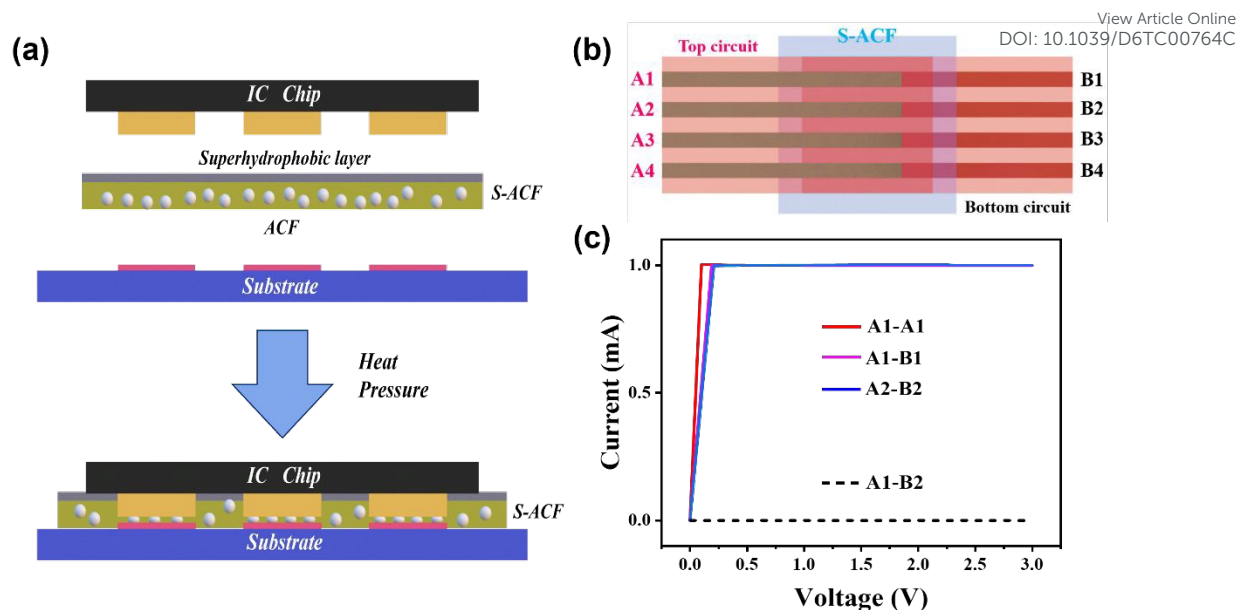
436 Figure 6a schematically illustrates the operating principle of the superhydrophobic
437 anisotropic conductive film in this study. The S-ACF is first laminated onto the
438 substrate and then hot-pressed at 0.3 MPa and 150 °C for 10 minutes. During pressing,
439 the Ag-coated SiO₂ microspheres (~10 μm in diameter, Figure S4c) readily penetrate
440 the ultrathin superhydrophobic top layer (~3 μm thick, Figure 2d), whose thickness is



441 substantially smaller than the particle diameter. This geometry minimizes interference
442 with electrical interconnection, consistent with the comparable initial contact
443 resistances of the base ACF (1.58 Ω) and S-ACF (1.64 Ω). The test circuit is shown in
444 Figure S3. Figure S8 and S9 display the surface and cross-section of the actual S-ACF
445 after hot pressing. It can be observed that the conductive particles penetrate the
446 hydrophobic layer, and the hydrophobic layer does not erode the interior of the base
447 ACF, confirming the conductive mechanism of the S-ACF. The superhydrophobic layer
448 that remains in non-contact regions after hot-pressing provides a continuous moisture
449 barrier, effectively suppressing aging and performance drift during operation.

450 To further evaluate the electrical performance, a test circuit comprising four parallel
451 Ag traces on two PI films was assembled (Figure 6b), with an electrode spacing of 1
452 mm. The S-ACF was hot-pressed at 0.3 MPa between aligned PI films (precisely
453 matching A1–A4 with B1–B4) and subsequently cured at 150 °C for 1 h. The current–
454 voltage (I–V) characteristics measured for the aligned electrode pairs exhibit stable and
455 reproducible electrical conduction, indicating that effective electrical pathways are
456 formed across the bonded interfaces (Figure 6c). Compared with the direct A1–A1
457 reference, the aligned A1–B1 and A2–B2 electrode pairs show a consistent conductive
458 response, reflecting the contribution of the bonded ACF layer while maintaining
459 reliable electrical connectivity. In contrast, the misaligned A1–B2 electrodes display
460 negligible current over the entire measurement range, demonstrating excellent electrical
461 insulation along the in-plane (X–Y) direction. This pronounced electrical anisotropy
462 confirms that conductive pathways are selectively established along the Z direction
463 during hot pressing, while lateral conduction is effectively suppressed. Such behavior
464 originates from the localized penetration of conductive particles under compression and
465 the absence of continuous conductive pathways in the in-plane direction, ensuring
466 effective Z-axis conduction together with robust X–Y insulation.





467

468 **Figure 6.** Electrical conductivity of the S-ACF. (a) Schematic of conductive pathways
 469 formed after hot pressing. (b) Circuit diagram for electrical measurement with the S-
 470 ACF sandwiched between silver electrodes. (c) Linear current-voltage (I-V) curve
 471 confirming ohmic conduction.

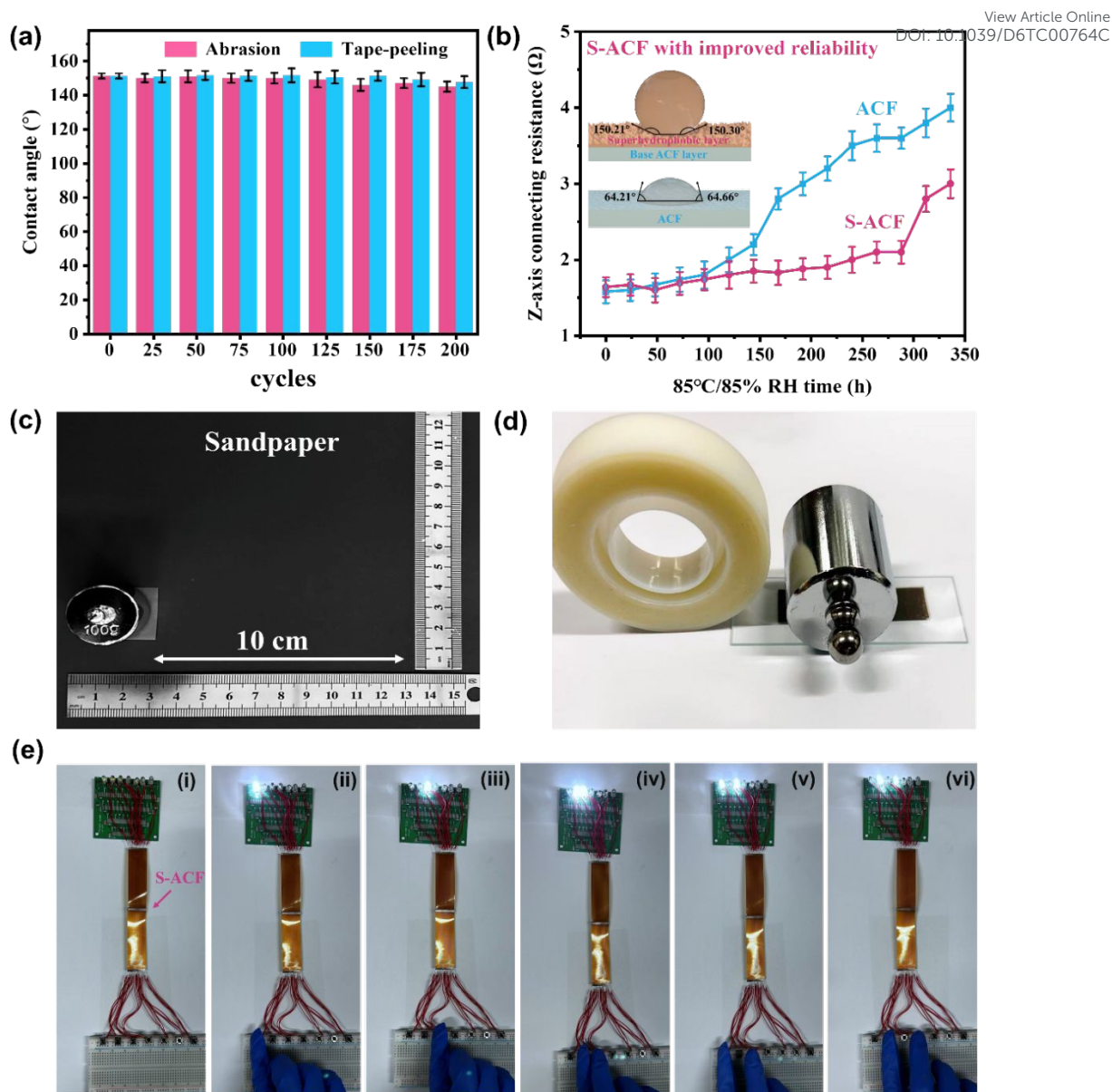
472 Figure 7 systematically evaluates the mechanical durability and humid-heat
 473 reliability of the superhydrophobic anisotropic conductive film in comparison to the
 474 conventional base ACF. Abrasion resistance was quantified using a linear reciprocating
 475 test under a 100 g load over a 10-cm path on sandpaper. In parallel, adhesion resilience
 476 was assessed via a tape-peel test, in which 3M tape was uniformly applied under a 200 g
 477 weight and peeled at a constant speed. Contact angle measurements performed during
 478 these tests revealed exceptional retention of superhydrophobicity: after 200 abrasion
 479 cycles, the S-ACF maintained a static contact angle above 145° , a drop of only 5° , while
 480 the tape-peel test resulted in a further decrease of merely 3° , yielding 147° (Figure 7a).
 481 This notable performance-reflecting negligible degradation of the micro-nano-
 482 structured hydrophobic surface-can be attributed to the viscoelastic SEBS matrix,
 483 which dissipates local shear and friction stresses at the micro-scale, as well as
 484 effectively anchors the gas-phase SiO_2 particles through an entrapment mechanism.
 485 Furthermore, the cross-linked epoxy network within the ACF matrix provides
 486 mechanical reinforcement and stabilizes the SEBS chains, thereby preventing particle



487 dislodgement. Such mechanical robustness helps preserve the integrity of the
488 superhydrophobic barrier. While the coating does not directly enhance the intrinsic
489 metal-epoxy bonding or particle-pad contact formation, it can slow moisture/ion ingress
490 and thereby indirectly mitigate degradation at these moisture-sensitive interfaces during
491 humid-heat exposure.

492 Electrical aging behavior further corroborates these findings. Figure 7b and Tables
493 S2 and S3 illustrate the trend of contact resistance changes during long-term aging
494 under accelerated humid heat conditions (85°C, 85% RH). Unmodified base ACF
495 exhibits a gradual increase in resistance followed by a sharp rise after 150 hours,
496 indicating persistent deterioration of the conductive path. In contrast, S-ACF
497 consistently maintained lower and more stable resistance values, showing significant
498 changes only after 300 hours-meaning it achieved twice the reliability improvement
499 over the base ACF in wet-heat aging tolerance. The mechanism behind this enhanced
500 wet-heat reliability lies in the accelerated diffusion of water molecules into the ACF
501 matrix under 85°C/85% RH aging conditions. In unmodified ACF, water vapor
502 permeates into the interior through pathways such as surface micro-protrusions,
503 interfaces, and voids, degrading electrical performance. S-ACF, however, benefits from
504 a dense, low-energy barrier layer formed by its vapor-phase SiO₂ micro-nano structure
505 coating. This layer obstructs vapor penetration through interfaces and voids, effectively
506 blocking moisture ingress and delaying degradation. This inhibits the rate of resistance
507 increase, extending the functional lifespan of electronic interconnects. From an
508 application perspective, these durability improvements translate directly into enhanced
509 device reliability by reducing repair frequency and extending service life under humid
510 conditions. The bilayer S-ACF is therefore well suited for electronic interconnects
511 exposed to moisture, condensation, or surface contamination, including foldable
512 displays, flexible sensor arrays, outdoor flexible electronics, and compact packaging
513 systems operating in high-humidity environments. Figure 7c and 7d present the
514 experimental photographs of the wear resistance and peel tests, respectively.



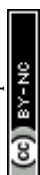


515

516 **Figure 7.** Durability and humid-heat reliability of the S-ACF. (a) Evolution of the water
 517 contact angle over cycles of abrasive wear and tape peeling. (b) Performance
 518 comparison of ACF and S-ACF during an accelerated aging test at 85 °C and 85%
 519 relative humidity (RH). For the 85 °C/85% RH aging test, ten independent specimens
 520 were tested for each group. (c) Abrasion resistance test procedure, where one cycle is
 521 defined as a 10-cm linear stroke and return. (d) Adhesive tape-peeling test setup. (e)
 522 Demonstration of reliable electrical function in a circuit interconnected with S-ACF,
 523 showing device operation with various switch activations: (i) all off, (ii) switch 1, (iii)
 524 switch 3, (iv) switches 2 & 3, (v) switches 1 & 3, (vi) switches 2 & 4.

525

To further validate the functional anisotropy of S-ACF, a circuit assembly was



526 constructed by connecting two FPC-200 circuit boards (each containing seven
527 independent circuits, the spacing between different electrodes is 1 mm.) via the S-ACF
528 layer. Each circuit integrates a touch switch, LED indicator (emitting white light, with
529 LED beads measuring 3 mm in size), and 3V power supply. As shown in Figure 7e,
530 pressing a specific touch switch illuminates only the corresponding LED without
531 crosstalk or false activation. More importantly, as shown in Figure S10a and S10b, we
532 employed PI film with an interdigitated electrode as the minimal lateral insulation test
533 circuit for the S-ACF. Each individual electrode strip features identical line widths, with
534 15 electrode pairs per strip. The increased number of electrodes effectively mitigates
535 random effects, enabling precise determination of the minimum spacing for lateral short
536 circuits in S-ACF. Test electrodes with line widths of 50, 60, 70, 80, 90, and 100 μm
537 between electrodes were prepared. The S-ACF was hot-pressed and cured onto the
538 electrodes for testing. Applying a 10V voltage between A and B electrodes revealed
539 that only the 50 and 60 μm spacing electrodes exhibited current flow (Figure S10b),
540 while the 70, 80, 90, and 100 μm spacing electrodes showed no current (due to testing
541 environment constraints, the maximum measurable current was limited to 10mA to
542 prevent instrument damage). This indicates that the minimum lateral insulation spacing
543 for S-ACF is approximately 60 μm , demonstrating excellent electrical isolation and
544 precise anisotropic conductivity.

545

546 4. Conclusions

547 In this study, a superhydrophobic anisotropic conductive film (S-ACF) was
548 fabricated via a spray coating process employing SiO_2 and SEBS to construct a dual-
549 layer architecture comprising a hydrophobic top layer and a conductive base. The S-
550 ACF exhibited a static water contact angle of 150° , markedly higher than the pristine
551 ACF (64°), thereby achieving superhydrophobicity. Mechanical integrity was fully
552 preserved: the bonding strength remained nearly unchanged (17.1 MPa vs. 17.2 MPa),
553 while tensile strength (4.93 MPa) and elongation at break (105%) were comparable to



554 those of the unmodified ACF (5.11 MPa and 100%). Electrical performance was
555 likewise maintained, with a Z-axis contact resistance of 1.64 Ω , similar to the original
556 ACF (1.58 Ω), and minimum lateral insulation with approximately 60 μm , confirming
557 that the thin hydrophobic layer does not hinder conductive pathways. Durability testing
558 further highlighted the robustness of the S-ACF: after 200 cycles of abrasion and tape-
559 peeling, the contact angle remained $\geq 145^\circ$, indicating strong retention of surface
560 hydrophobicity. Under accelerated aging (85 $^\circ\text{C}/85\%$ RH), the resistance inflection
561 point shifted from ~ 150 h to ~ 300 h, demonstrating a twofold humid-heat reliability
562 improvement in humid heat stability. Overall, this bilayer design synergistically
563 optimizes hydrophobicity, electrical conductivity, mechanical strength, and
564 environmental resilience, providing a practical and scalable strategy for developing
565 high-performance ACFs in moisture-sensitive and flexible electronic applications.

566 **Author contributions**

567 W.Z.: Methodology, Investigation, Data curation, Writing—original draft. G.Z.:
568 Investigation, Data curation. P.L.: Methodology, Investigation, Data curation,
569 Supervision. Funding acquisition, Resources, Project administration, Writing – review
570 & editing. L.H.: Methodology, Data curation. W.Z.: Investigation, Data curation. L.L.:
571 Resources. H.L.: Resources. Q.Z.: Resources. Z.G.: Resources, Writing – review &
572 editing. X.L.: Resources, Project administration, Writing – review & editing. Figure 1
573 by figdraw.com

574 **Conflicts of interest**

575 The authors declare no conflict of interest.

576 **Acknowledgements**

577 This work was financially supported by the National Natural Science Foundation of
578 China (No. 22575181 and No. 22404130). The authors also acknowledge the
579 Fundamental Research Funds for the Central Universities (No. ZYTS25238), Xidian



580 University Specially Funded Project for Interdisciplinary Exploration (No.
581 TZJH2024042), the Postgraduate Innovation Fund of Xidian University, and the
582 support from King Abdullah University of Science and Technology.

583 References

- 584 1. S. Sadeghi, R. B. Canty, N. Mukhin, J. Xu, F. Delgado-Licona and M.
585 Abolhasani, Engineering a sustainable future: Harnessing automation, robotics,
586 and artificial intelligence with self-driving laboratories, *ACS Sustain. Chem.*
587 *Eng.*, 2024, **12**, 12695-12707.
- 588 2. J. Jiang, H. Gu, R. Xu, J. Zhou, Y. Gao, L. Zhang, X. Cong, Y. Jiang and L.
589 Song, Deep Learning-Assisted 3D Pressure Sensors for Control of Unmanned
590 Aerial Vehicles, *ACS Appl. Mater. Interfaces*, 2025, **17**, 31107-31117.
- 591 3. Z. Wang, K. Wang, Y. Liu, X. Guan, Z. Pan, Y. Yao and T. Li, Triboelectric
592 Sensor with a Hierarchical Structure for Omnidirectional Adaptive Wind Speed
593 and Wind Direction Sensing for Unmanned Aerial Vehicles, *ACS Appl. Mater.*
594 *Interfaces*, 2025, **17**, 23984-23995.
- 595 4. J. E. Ryu, S. Park, Y. Park, S. W. Ryu, K. Hwang and H. W. J. A. M. Jang,
596 Technological breakthroughs in chip fabrication, transfer, and color conversion
597 for high-performance micro-LED displays, *Adv. Mater.*, 2023, **35**, 2204947.
- 598 5. S. K. Paral, J.-Y. Jeng, C.-H. Wu, G.-W. Lin, Y.-L. Cheng and D.-Z. J. A. S. S.
599 Lin, Nanoscale roughness to mitigate polydimethylsiloxane (PDMS) sticking in
600 liquid crystal display (LCD) vat photopolymerization (VPP): Separation force
601 reduction without losing resolution, *Appl. Surf. Sci.*, 2025, **683**, 161773.
- 602 6. K. M. Lee, N. Kim, J. K. Lee, H. J. Lee, S. Y. Kim and T. G. J. A. S. S. Kim,
603 Mesh-patterned IZO/Hf-doped IGZO thin film transistors with high mobility
604 and mechanical stability for flexible display, *Appl. Surf. Sci.*, 2025, **686**,
605 162102.
- 606 7. P. Jastrzebska-Perfect, Spyropoulos, G. D., Cea, C., Zhao, Z., Rauhala, O. J.,
607 Viswanathan, A., Khodagholy, D., Mixed-conducting particulate composites



- 608 for soft electronics, *Sci. Adv.*, 2020, **6**, eaaz6767.
- 609 8. C. Xu, S. Guan, H. Zhang, W. Fan, X. Zhuang and X. Dong, Hierarchical hybrid
610 crosslinking multifunctional gelatin-based hydrogel: ideal platforms for flexible
611 wearable devices, brain–computer interfaces and biomedical applications, *J.*
612 *Mater. Chem. A*, 2025, **13**, 450-459.
- 613 9. D. H. Choi, H. T. Kim, Y. Kim, K. Park, M. S. Kim, J. H. Lee, G. I. Kim, J. J.
614 Chung and H. J. J. A. S. S. Kim, Nature-derived, biocompatible silibinin based
615 bioresorbable neuromorphic device for implantable medical electronics, *Appl.*
616 *Surf. Sci.*, 2023, **621**, 156814.
- 617 10. D. Ge, H.-Y. Yu, Z. Miao, X. He and S. Y. H. Abdalkarim, Intrinsically
618 conductive bifunctional nanocellulose-reinforced robust and self-healable
619 electronic skin: deep insights into multiple bonding network, property
620 reinforcement, and sensing mechanism, *ACS Sustain. Chem. Eng.*, 2022, **11**,
621 1157-1167.
- 622 11. L. Chen, Y. Xu, Y. Liu, J. Wang, J. Chen, X. Chang and Y. Zhu, Flexible and
623 transparent electronic skin sensor with sensing capabilities for pressure,
624 temperature, and humidity, *ACS Appl. Mater. Interfaces*, 2023, **15**, 24923-
625 24932.
- 626 12. T. Chen, P. Wei, G. Chen, H. Liu, I. T. Mugaanire, K. Hou and M. Zhu,
627 Heterogeneous structured tough conductive gel fibres for stable and high-
628 performance wearable strain sensors, *J. Mater. Chem. A*, 2021, **9**, 12265-12275.
- 629 13. H. R. Ansari, A. Mirzaei, H. Shokrollahi, R. Kumar, J.-Y. Kim, H. W. Kim, M.
630 Kumar and S. S. Kim, Flexible/wearable resistive gas sensors based on 2D
631 materials, *J. Mater. Chem. C*, 2023, **11**, 6528-6549.
- 632 14. X. Jiang, Y. Cheng, L. Shi, J. Sun and R. Wang, A soft, fatigue-free, and self-
633 healable ionic elastomer via the synergy of skin-like assembly and Bouligand
634 structure, *Angew. Chem., Int. Ed.*, 2024, **63**, e202411418.
- 635 15. W. Hong, X. Guo, T. Zhang, S. Mu, F. Wu, Z. Yan, H. Zhang, X. Li, A. Zhang
636 and J. Wang, Flexible strain sensor based on nickel microparticles/carbon black
637 microspheres/polydimethylsiloxane conductive composites for human motion



- 638 detection, *ACS Appl. Mater. Interfaces*, 2024, **16**, 32702-32712. View Article Online
DOI: 10.1039/D6TC00764C
- 639 16. J. Li, Y. Duan, H. Cao, Y. Wang, X. Lu, Y. Xu, R. Sun and Y. Hu, Pressure-
640 adaptive core-shell liquid metal microspheres for reliable flip-chip
641 interconnects, *Chem. Eng. J.*, 2025, **520**, 165694.
- 642 17. C.-K. Huang, C.-Y. Chiu, T.-L. Lai, C. Cheng, W.-H. Lai, P.-J. Chang, J.-L.
643 Wu, C.-H. Chiang, C.-G. Wu and C.-Y. Liu, Flip-chip packaged perovskite
644 solar cells, *Energy Technol.*, 2021, **9**, 2001129.
- 645 18. S. Jiang, X. Liu, J. Liu, D. Ye, Y. Duan, K. Li, Z. Yin and Y. Huang, Flexible
646 metamaterial electronics, *Adv. Mater.*, 2022, **34**, 2200070.
- 647 19. J. H. Lee, K. Cho and J. K. J. A. M. Kim, Age of flexible electronics: emerging
648 trends in soft multifunctional sensors, *Adv. Mater.*, 2024, **36**, 2310505.
- 649 20. H. Hwang, M. Kong, K. Kim, D. Park, S. Lee, S. Park, H.-J. Song and U. Jeong,
650 Stretchable anisotropic conductive film (S-ACF) for electrical interfacing in
651 high-resolution stretchable circuits, *Sci. Adv*, 2021, **7**, eabh0171.
- 652 21. Y. Liu, Y. Pan, Z. Zheng, H. Zhang, R. Sun and P. Zhu, A sandwich-structured
653 anisotropic conductive film with robust interfacial reliability and conductivity
654 for functional electrical interconnections, *Chem. Eng. J.*, 2025, **505**, 159721.
- 655 22. Q. Liu, Y. Shi, Q. Pan, D. Yang, Y. Lan, Z. Chen and T. J. A. S. S. Wang,
656 Bioinspired surface engineering of multifunctional tea polyphenols towards
657 ambient fabrication of Cu@ Ni nanowire flexible transparent conductive films,
658 *Appl. Surf. Sci.*, 2025, **715**, 164600.
- 659 23. Y. Chen, C. Hao, H. Zhang, W. Xue, S. Cai, C. Jiang, Z. Xiao, G. Cao and Y.
660 Tian, The preparation of polystyrene/nickel core-shell particles for anisotropic
661 conductive films (ACFs), *Prog. Org. Coat.*, 2024, **195**, 108662.
- 662 24. P. Rytlewski, P. Augustyn, R. Malinowski, B. Budner and A. J. A. S. S.
663 Antończak, Surface metallisation of acrylonitrile-butadiene-styrene (ABS)
664 composites via a novel electroplating technique, *Appl. Surf. Sci.*, 2025, **712**,
665 164146.
- 666 25. W. Zhang, Y. Zhou, Y. Ding, L. Song, Q. Yuan, W. Zhao, C. Xu, J. Wei, M. Li
667 and H. J. A. S. S. Ji, Sintering mechanism of size-controllable Cu-Ag core-shell

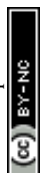


- 668 nanoparticles for flexible conductive film with high conductivity, antioxidant,
669 and electrochemical migration resistance, *Appl. Surf. Sci.*, 2022, **586**, 152691.
- 670 26. A. Cao, Y. Gong, D. Liu, F. Yang, Y. Fan, Y. Guo, X. Tian and Y. Li, Rapid
671 fabrication of gold microsphere arrays with stable deep-pressing anisotropic
672 conductivity for advanced packaging, *Nat Commun*, 2024, **15**, 9182.
- 673 27. D. Park, H. Kwak, S. Kim, H. Choi, I. Lim, M. Kwak, I. S. Kim, H. Park, I. Y.
674 Eom, J. W. Lee, I. Park, A. Lee and U. Jeong, Stretchable Anisotropic
675 Conductive Film with Position-Registered Conductive Microparticles Used for
676 Strain-Insensitive Ionic Interfacing in Stretchable Ionic Sensors, *Adv. Funct.
677 Mater.*, 2024, **34**, 2408902.
- 678 28. C. Hao, J. Chen, Y. Chen, C. Jiang, Z. Wang, T. Pan, X. Cheng and Y. Tian,
679 Preparation of silver-coated polystyrene microspheres intermediated with
680 polyaniline and their application in array-patterned anisotropic conductive films,
681 *Adv. Compos. Hybrid Mater.*, 2024, **8**, 67.
- 682 29. D. Wang, Z. Ma, Z. Han, K. Wu, Y. Liu and X. Tian, Synthesis of high-
683 temperature hydrophobic nanoparticles and their applications in superlyophobic
684 coatings, *J. Mater. Chem. A*, 2025, **13**, 33264-33275.
- 685 30. J. S. Arya, M. K. Mahato, S. Sankararaman and E. Prasad, Conducting and
686 superhydrophobic hybrid 2D material from coronene and pyrene, *J. Mater.
687 Chem. C*, 2021, **9**, 10324-10333.
- 688 31. X. Yan, B. Ji, L. Feng, X. Wang, D. Yang, K. F. Rabbi, Q. Peng, M. J. Hoque,
689 P. Jin and E. J. A. n. Bello, Particulate–droplet coalescence and self-transport
690 on superhydrophobic surfaces, *ACS nano*, 2022, **16**, 12910-12921.
- 691 32. X. Liu, P. Wang, D. Zhang and X. Chen, Atmospheric corrosion protection
692 performance and mechanism of superhydrophobic surface based on
693 coalescence-induced droplet self-jumping behavior, *ACS Appl. Mater.
694 Interfaces*, 2021, **13**, 25438-25450.
- 695 33. Z. Jin, H. Mei, L. Pan, H. Liu and L. Cheng, Superhydrophobic Self-Cleaning
696 Hierarchical Micro-/Nanocomposite Coating with High Corrosion Resistance
697 and Durability, *ACS Sustain. Chem. Eng.*, 2021, **9**, 4111-4121.



- 698 34. S. Wang, Z. Zhao, Q. Yu, P. Li, F. Zhou, C. Xu, X. Zhao and Y. Teng, *View Article Online*
699 Superdurable Full-Life Superhydrophobic Composite Block, *Adv. Mater.*, 2024, *DOI: 10.1039/D6TC00764C*
700 **36**, e2403853.
- 701 35. J. Zhang, Y. Chen, Y. Zhang, S. Wu, J. Sun, X. Liu and J. Song, Fabrication
702 and Energy Collection of Superhydrophobic Ultra-Stretchable Film, *Adv. Funct.*
703 *Mater.*, 2024, **34**, 2400024.
- 704 36. G. Zhang, P. Li, W. Zhao, Y. Wang, L. Zhang, J. Shi, C. Su, W. Du, Z. Li and
705 X. Liu, MXene Nanofluid-Driven Interfacial Synergy for Next-Generation
706 Anisotropic Conductive Films, *ACS Appl. Mater. Interfaces*, 2025, **17**, 55161–
707 55171.
- 708 37. S. A. o. C. (SAC), 2008.
- 709 38. G. T. 2567-2008, Test methods for properties of resin casting boby, 2008.
- 710 39. C. M. Cormican, S. Bektaş, F. J. Martin-Martinez and S. J. A. M. Alexander,
711 Emerging trends in bioinspired superhydrophobic and superoleophobic
712 sustainable surfaces, *Adv. Mater.*, 2025, **37**, 2415961.
- 713 40. C. Ye, D. Liu, X. Peng, Y. Jiang, R. Cheng, C. Ning, F. Sheng, Y. Zhang, K.
714 Dong and Z. L. J. A. N. Wang, A hydrophobic self-repairing power textile for
715 effective water droplet energy harvesting, *Acs Nano*, 2021, **15**, 18172-18181.
- 716 41. F. Wang, J. Pi, F. Song, R. Feng, C. Xu, X.-L. Wang and Y.-Z. Wang, A
717 superhydrophobic coating to create multi-functional materials with
718 mechanical/chemical/physical robustness, *Chem. Eng. J.*, 2020, **381**, 122539.

719



The data supporting this article have been included as part of the **Supplementary Information**.

